Band alignment of two-dimensional semiconductors for designing heterostructures with momentum space matching

V. Ongun Özçelik,[1,*] Javad G. Azadani,[2] Ce Yang,[3] Steven J. Koester,[2] and Tony Low[2,†]
[1]*Andlinger Center for Energy and the Environment, Princeton University, Princeton, New Jersey 08544, USA*
[2]*Department of Electrical and Computer Engineering, University of Minnesota, Minneapolis, Minnesota 55455, USA*
[3]*Institute of Microelectronics, Peking University, Beijing, China*
(Received 23 March 2016; revised manuscript received 10 May 2016; published 11 July 2016)

We present a comprehensive study of the band alignments of two-dimensional (2D) semiconducting materials and highlight the possibilities of forming momentum-matched type I, II, and III heterostructures, an enticing possibility being atomic heterostructures where the constituent monolayers have band edges at the zone center, i.e., Γ valley. Our study, which includes the group IV and III-V compound monolayer materials, group V elemental monolayer materials, transition-metal dichalcogenides, and transition-metal trichalcogenides, reveals that almost half of these materials have conduction and/or valence band edges residing at the zone center. Using first-principles density functional calculations, we present the type of the heterostructure for 903 different possible combinations of these 2D materials which establishes a periodic table of heterostructures.

DOI: 10.1103/PhysRevB.94.035125

I. INTRODUCTION

Semiconductors have been at the heart of some of the most transformative device innovations over the course of the last 50 years, and research in two-dimensional (2D) atomic crystals has recently begun to focus on their heterostructures [1,2]. This includes heterostructures of graphene [3,4], which were followed by other monolayer structures each with different exceptional properties such as the insulator boron nitride [5,6], silicene and germanene which are the silicon and germanium based analogs of graphene [7–9], oxygenated monolayers of graphene [10] and silicene [11,12], and transition-metal dichalcogenides (TMDs) [13–16]. Concomitantly, there are hundreds of different 2D materials and their permutations amount to numerous combinations of heterostructures. Certainly, theoretical exploration of these materials is needed to identify promising atomic heterostructures for device applications since depending on the field of usage, the requirements for heterostructures' band alignments change.

According to their bands alignments, heterostructures can be classified into three types, i.e., type I (symmetric), type II (staggered), or type III (broken), as described in Fig. 1. Each of these band alignments has particular applications to enable different varieties of devices. Type I band alignments are most widely utilized in optical devices, such as light-emitting diodes (LEDs) [17] and in lasers as they provide a means to spatially confine electrons and holes so that efficient recombination can occur. The ability to fabricate single and multiple quantum wells has further enhanced the performance of lasers and LED devices [18,19]. Type II band alignments are very useful for unipolar electronic device applications since they allow larger offsets on one side (either conduction or valence band), thus allowing extremely strong carrier confinement. Type II high electron mobility transistors (HEMTs) based on InAs/AlSb quantum wells are excellent examples of the strong carrier confinement that can be achieved in type II heterostructures [20]. Conduction band notches can also be used as hot electron injectors in bipolar transistors [21] and as quantum well resonant tunneling bipolar transistors [22]. Type II and type III heterostructures are also useful to engineer the conduction to valence band transition energy. This is particularly important in tunneling field effect transistors (TFETs) in order to enhance the tunneling current density [23], as well as in infrared intersubband superlattice lasers [24] and wavelength photodetectors [25]. Perhaps some of the most impressive devices enabled by semiconductor heterostructures are quantum cascade lasers, which use complex heterostructure stacks to engineer minibands and intrasubband transitions which allow efficient light emission from the mid-infrared to the terahertz regimes [26]. Many optical device concepts have also been proposed or realized using 2D materials. Atomically thin pn diodes of type II heterostructures have recently been demonstrated to exhibit current rectification and collection of photoexcited carriers [27]. The latter can also be achieved using graphene/TMD/graphene heterostructures [28]. Phototransistor structures based on graphene/MoS_2 which exhibit ultrahigh gain have also been realized [29]. Light-emitting diodes based on type I heterostructures with the TMD sandwiched between BN and graphene as contacts can also be engineered across a wide spectral range [30]. Very recently, type II heterostructures have also been explored as a platform for harnessing long-lived interlayer (or indirect) excitons [31,32]. Additionally, lateral heterostructures of TMDs with other classes of monolayer materials can be utilized for various applications [33–36].

Due to their extensive functionalities as described above, the electronic band structures of 2D materials and their band gap engineering have been the focus of many recent studies. However, their relative band alignments (band offsets) have not been fully explored yet, except for the more common 2D materials such as graphene, BN, and some TMDs [37–39]. As far as heterostructures are concerned, the relative band alignment of semiconductors is one of the most important parameters of design since it identifies the type of the heterostructure. In addition, in all of the above-mentioned devices, just as in their 3D counterparts, it is critical for the conduction and/or

*ongun@princeton.edu
†tlow@umn.edu

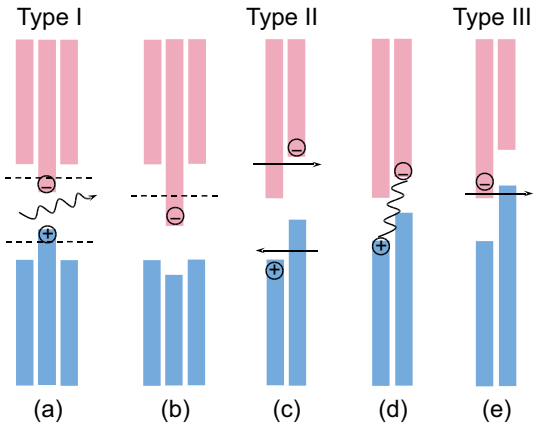

FIG. 1. Illustration of type I, II, and III heterostructures and their various devices, where red (blue) indicates conduction (valence) bands. (a) Laser utilizing type I heterostructure. (b) High electron mobility transistor, (c) carrier separation in solar cell, and (d) interlayer excitons utilizing type II junction. (e) Tunneling field effect transistor based on type III junction. Specifically, when material A and material B merge, the resulting heterostructure is type I if $VBM_A<VBM_B<CBM_B<CBM_A$; is type II if $VBM_A<VBM_B<CBM_A<CBM_B$; and type III if $VBM_A<CBM_A<VBM_B<CBM_B$.

valence band edges of constituent heterostructure materials to be momentum-matched. For instance, due to the inherent likelihood for some degree of misorientation in 2D layered stacks, and the desire to combine a highly diverse set of materials, 2D materials with band edges at the zone center (Γ point) point are extremely attractive, since momentum space matching problems can largely be eliminated through the use of these materials.

In this paper, motivated by the emergence of 2D heterostructures as the next generation materials and the importance of comparative information of their band alignment and momentum matching for designing heterostructures, we perform a comprehensive study of well-known 2D semiconducting materials, presenting their band edge properties and discussing the possibilities for forming momentum-matched heterostructures. Hence, our survey with density functional theory (DFT) calculations includes various classes of 2D semiconductors such as group IV and III-V compound monolayer materials, group V elemental monolayer materials, TMDs, and transition-metal trichalcogenides (TMTs). For each class of semiconductors, we present the types of stable geometrical phases, structural dimensions, the electronic band structures, locations of the valance band maximum (VBM) and conduction band minimum (CBM) calculated with reference to vacuum in the momentum space, the values of the electronic affinities, and the type of the band gap. These results establish a complete comparative database of 2D semiconductor materials whose band alignments and electronic properties are calculated using a unified approach. Following this, we calculate the type of the heterostructure for each possible combination of these 2D materials which results in a periodic table of heterostructures. Thus, our paper presents a comprehensive library for determining the type of the heterostructure that will appear when two monolayer semiconductors are merged together.

II. METHOD

We performed first-principles pseudopotential calculations based on the spin-polarized DFT within the generalized gradient approximation including van der Waals corrections [40] and spin-orbit coupling. We used projector-augmented wave potentials [41] and approximated the exchange-correlation potential with the Perdew-Burke-Ernzerhof (PBE) functional [42]. We sampled the Brillouin zone (BZ) in the Monkhorst-Pack scheme, and tested the convergence in energy as a function of the number of **k** points for the calculations. The **k**-point sampling of $(21\times21\times1)$ was found to be suitable for the BZ corresponding to the primitive unit cell. Atomic positions were optimized using the conjugate gradient method, where the total energy and atomic forces were minimized. The energy convergence value between two consecutive steps was chosen as 10^{-6} eV. Numerical calculations were carried out using the VASP software [43], where the "PREC=Accurate" setting was used for structural minimization. Since the band gaps are usually underestimated by DFT, we also performed calculations using the HSE06 hybrid functional [44], which is constructed by mixing 25% of the Fock exchange with 75% of the PBE exchange and 100% of the PBE correlation energy. Electronic calculations at the HSE06 level were performed using the structures that were relaxed using PBE. Hence, our PBE and HSE06 results constitute our lower and upper bound estimates of the electronic gaps. The monolayer structures examined in this study were previously shown to be stable by means of phonon dispersion curves, high-temperature molecular dynamics simulations, or by experimental data, where relevant citations are given in the following sections for each group of materials. Throughout this work we present all of the energy values with reference to the vacuum energy, which we extracted from the local potential distribution within the unit cell. Thus, vacuum energies are set to zero in the band alignment figures. It should be noted that monolayer semiconductors for which materials are found to be metallic are not presented here.

III. BAND ALIGNMENTS

A. Group IV and III-V compound materials

After the exfoliation of hexagonal boron nitride monolayers [5,45], the search for similar group IV and III-V compound materials and designing nanoscale devices composed of their heterostructures has drawn considerable attention [46–50]. It is possible to separate these materials into two distinct groups depending on their stable geometries [51]. The compounds in the first group (namely, BN, BP, BAs, BSb,AlN, AlP, AlAs, GaN, InN, SiC, GeC, SnC) have the same hexagonal honeycomb structure similar to graphene but with different lattice constants. Among these, BN is most closely lattice matched with graphene having a lattice constant of 1.45 Å (versus 1.42 Å for graphene), but with ionic bonds and a wide band gap as opposed to the zero band gap graphene. The other stable structure that group IV and III-V compounds possess is the buckled geometry where the adjacent atoms of

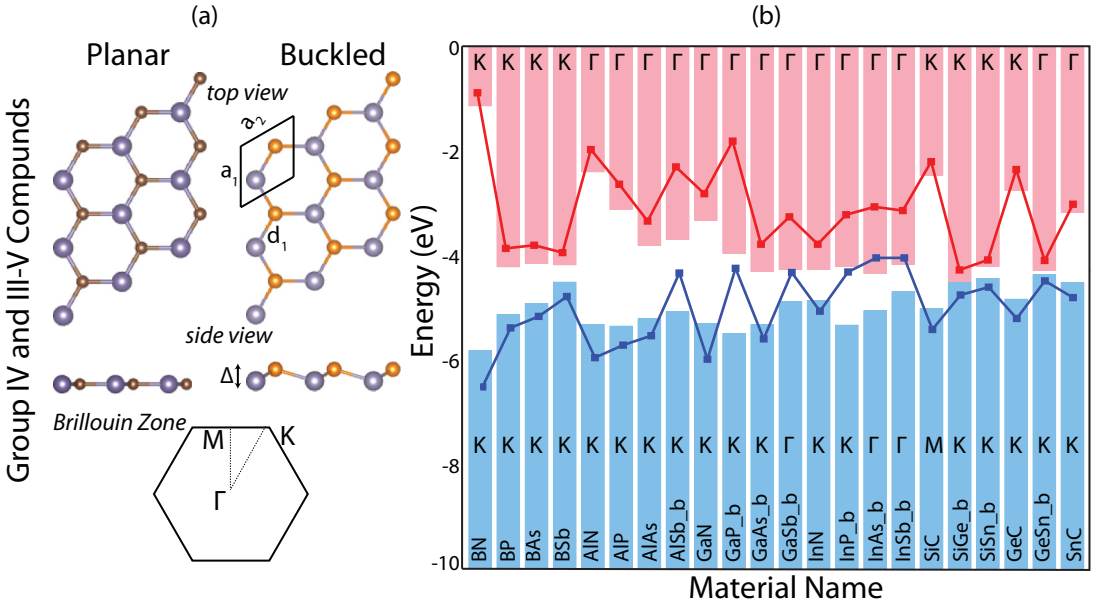

FIG. 2. (a) Stable crystalline structures (planar and buckled) of group IV and group III-V monolayer compounds and their hexagonal BZ with high-symmetry points are shown. The relevant bond lengths, lattice parameter, and buckling distance are indicated by a, d, and Δ, respectively. (b) Comparative band alignment of group IV and group III-V monolayer compounds where CBM (shown in red) and VBM (shown in blue) values obtained from PBE and HSE06 calculations are shown with bar and line plots, respectively. The positions of CBM and VBM on the BZ are indicated. Note that the vacuum energies were set to zero while calculating the band diagrams. Structures having buckled (b), puckered (w), 2H, 1T, and distorted 1T phases are indicated with the corresponding indices, where no index is used for planar phases.

the material are in two parallel planes separated by a buckling distance (Δ) in the vertical direction, as shown in Fig. 2(a). It should be noted that compounds with a buckled geometry (namely, AlSb, GaP, GaAs, GaSb, InP, InAs, InSb, SiGe, SiSn, GeSn) do not contain an element from the second row of the periodic table (as opposed to planar structures) and their stability is maintained by the buckling of the bonds. Despite this buckling in the vertical direction, these materials maintain their hexagonal symmetries and all have the same hexagonal BZ as their planar counterparts.

Monolayers of group IV and III-V compounds include a variety of different band alignments ranging from direct to indirect gap semiconductors with VBM and CBM at the K, Γ, and M points in momentum space, as illustrated in Fig. 2(b). There are also wide-band-gap insulators among these materials such as BN, AlN, and SiC. As a general trend, the VBM (CBM) increases (decreases) as the row numbers of the elements in the compounds increase, resulting in a corresponding decrease in the band gap. Among these, GaN and AlN, which have similar lattice constants, are attractive candidates for both lateral and vertical heterostructures. Additionally, buckled compounds of AlSb, GaP, GaSb, InP, InAs, and InSb have very high VBM, approaching −4 eV. These can be combined with low-CBM materials to form type III heterostructures. Also, large-gap compounds, such as BN, are natural candidates to combine with smaller-gap compounds (such as SiGe) to achieve a type I heterostructure. Specific candidates can be identified using the complete set of data presented in Table I.

B. Group V monolayers

Recently, another class of 2D materials, the group V monolayers, has also garnered attention in the community. Specially, the demonstration of field effect transistors using multilayers of black phosphorene [52,53] and related theoretical studies [54–56] have brought group V elements into focus. More recently, theoretical and experimental studies have been performed to explore the possible stable phases of other group V elements such as nitrogen, antimony, arsenic, and bismuth [57–61]. Reported high-temperature molecular dynamics simulations and DFT calculations in these previous studies show the existence of two distinct geometries. As shown in Fig. 3(a), the first geometry is the buckled structure similar to that observed in some group IV and III-V compounds. All of the group V elements have a stable monolayer phase in this buckled geometry. Among these, monolayer nitrogen (or nitrogene) is a wide-band-gap insulator with a fundamental direct band gap of 4.0 eV between Γ and M symmetry points. However, this band gap increases to 5.9 eV when calculated by the HSE06 funcional [44]. Similarly, the buckled structure of phosphorous, namely blue phosphorene [53,54], also has a direct band gap between Γ and M symmetry points, with a value of 1.98 eV which increases to 2.73 eV upon HSE06 corrections. In contrast to buckled nitrogene and phosphorene, the buckled monolayers of arsenic and antimony (arsenene and antimonene) have indirect band gaps. Apart from these buckled structures, phosphorene, arsenene, and antimonene have a different form of stable monolayer, namely the washboard (or puckered) geometry, which is also illustrated in Fig. 3(a). This is the phosphorene phase that most experiments reported recently as black phosphorene [52,53,62,63]. In the puckered phase, the structures lose their hexagonal symmetries and both their unit cell and BZ become rectangular. When stabilized in this geometry, the band gaps of phosphorene and arsenene decrease

TABLE I. Relevant lattice constants, bond lengths, buckling distance, VBM, and CBM values for heterostructures studied are shown. Structures having buckled (b), puckered (w), 2H, 1T, and distorted 1T phases are indicated with the corresponding indices, where no index is used for planar phases. The listed geometrical parameters are illustrated in Figs. 2, 3, 4, and 5. The VBM and CBM values calculated with HSE are also shown in parentheses.

Material	Lattice Constants (Å)	Bond Lengths (Å)	Buckling (Å)	VBM (eV)	CBM(eV)
BN	$a_1 = a_2 = 2.51$	$d_1 = 1.45$	$\Delta = 0$	−5.80 (−6.56)	−1.14 (−0.88)
BP	$a_1 = a_2 = 3.21$	$d_1 = 1.85$	$\Delta = 0$	−5.08 (−5.43)	−4.18 (−3.84)
BAs	$a_1 = a_2 = 3.39$	$d_1 = 1.96$	$\Delta = 0$	−4.89 (−5.21)	−4.13 (−3.78)
BSb	$a_1 = a_2 = 3.73$	$d_1 = 2.15$	$\Delta = 0$	−4.49 (−4.83)	−4.17 (−3.92)
AlN	$a_1 = a_2 = 3.12$	$d_1 = 1.80$	$\Delta = 0$	−5.29 (−6.00)	−2.38 (−1.96)
AlP	$a_1 = a_2 = 3.95$	$d_1 = 2.28$	$\Delta = 0$	−5.32 (−5.76)	−3.09 (−2.62)
AlAs	$a_1 = a_2 = 4.07$	$d_1 = 2.35$	$\Delta = 0$	−5.16 (−5.58)	−3.76 (−3.23)
AlSb_b	$a_1 = a_2 = 4.41$	$d_1 = 2.62$	$\Delta = 0.62$	−5.02 (−4.38)	−3.64 (−2.29)
GaN	$a_1 = a_2 = 3.25$	$d_1 = 1.88$	$\Delta = 0$	−5.24 (−6.03)	−3.27 (−2.80)
GaP_b	$a_1 = a_2 = 3.89$	$d_1 = 2.30$	$\Delta = 0.48$	−5.46 (−4.29)	−3.93 (−1.80)
GaAs_b	$a_1 = a_2 = 4.04$	$d_1 = 2.41$	$\Delta = 0.61$	−5.27 (−5.64)	−4.25 (−3.76)
GaSb_b	$a_1 = a_2 = 4.43$	$d_1 = 2.64$	$\Delta = 0.68$	−4.85 (−4.37)	−4.24 (−3.24)
InN	$a_1 = a_2 = 3.58$	$d_1 = 2.06$	$\Delta = 0$	−4.81 (−5.11)	−4.23 (−3.76)
InP_b	$a_1 = a_2 = 4.27$	$d_1 = 2.53$	$\Delta = 0.56$	−5.32 (−4.36)	−4.21 (−3.20)
InAs_b	$a_1 = a_2 = 4.35$	$d_1 = 2.61$	$\Delta = 0.71$	−5.02 (−4.09)	−4.31 (−3.05)
InSb_b	$a_1 = a_2 = 4.66$	$d_1 = 2.80$	$\Delta = 0.77$	−4.68 (−4.09)	−4.16 (−3.12)
SiC	$a_1 = a_2 = 3.09$	$d_1 = 1.78$	$\Delta = 0$	−5.01 (−5.46)	−2.46 (−2.19)
SiGe_b	$a_1 = a_2 = 3.94$	$d_1 = 2.35$	$\Delta = 0.60$	−4.52 (−4.80)	−4.51 (−4.25)
SiSn_b	$a_1 = a_2 = 4.26$	$d_1 = 2.55$	$\Delta = 0.69$	−4.43 (−4.65)	−4.21 (−4.06)
GeC	$a_1 = a_2 = 3.25$	$d_1 = 1.88$	$\Delta = 0$	−4.81 (−5.25)	−2.73 (−2.34)
GeSn_b	$a_1 = a_2 = 4.42$	$d_1 = 2.66$	$\Delta = 0.75$	−4.35 (−4.53)	−4.27 (−4.07)
SnC	$a_1 = a_2 = 3.58$	$d_1 = 2.07$	$\Delta = 0$	−4.51 (−4.85)	−3.53 (−3.00)
N_b	$a_1 = a_2 = 2.27$	$d_1 = 1.49$	$\Delta = 0.70$	−7.66 (−8.68)	−3.57 (−2.67)
P_b	$a_1 = a_2 = 3.28$	$d_1 = 2.26$	$\Delta = 1.24$	−6.09 (−6.54)	−4.11 (−3.81)
P_w	$a_1 = 4.55; a_2 = 3.31$	$d_1 = 2.22; d_2 = 3.52$	$\Delta = 2.11$	−4.87 (−5.51)	−4.01 (−3.98)
As_b	$a_1 = a_2 = 3.61$	$d_1 = 2.51$	$\Delta = 1.40$	−5.13 (−5.54)	−3.95 (−3.48)
As_w	$a_1 = 4.72; a_2 = 3.67$	$d_1 = 2.51; d_2 = 3.84$	$\Delta = 2.41$	−4.41 (−4.96)	−3.86 (−3.71)
Sb_b	$a_1 = a_2 = 4.04$	$d_1 = 2.87$	$\Delta = 1.68$	−4.24 (−4.48)	−3.46 (−3.26)
2H-MoS_2	$a_1 = a_2 = 3.19$	$d_1 = 2.41; d_2 = 4.00$		−5.84 (−6.33)	−4.25 (−4.18)
2H-$MoSe_2$	$a_1 = a_2 = 3.32$	$d_1 = 2.54; d_2 = 4.18$		−5.13 (−5.54)	−3.79 (−3.67)
2H-$MoTe_2$	$a_1 = a_2 = 3.55$	$d_1 = 2.73; d_2 = 4.48$		−4.64 (−5.09)	−3.68 (−3.62)
2H-WS_2	$a_1 = a_2 = 3.19$	$d_1 = 2.42; d_2 = 4.00$		−5.36 (−5.86)	−3.82 (−3.77)
2H-WSe_2	$a_1 = a_2 = 3.32$	$d_1 = 2.55; d_2 = 4.19$		−4.70 (−5.12)	−3.47 (−3.37)
2H-WTe_2	$a_1 = a_2 = 3.56$	$d_1 = 2.74; d_2 = 4.49$		−4.29 (−4.46)	−3.55 (−3.25)
1T-HfS_2	$a_1 = a_2 = 3.64$	$d_1 = 2.55; d_2 = 4.45$		−6.18 (−6.74)	−4.95 (−4.75)
1T-$HfSe_2$	$a_1 = a_2 = 3.76$	$d_1 = 2.68; d_2 = 4.62$		−5.33 (−5.76)	−4.93 (−4.74)
1T_d-ReS_2	$a_1 = 6.38; a_2 = 6.47$	$d_1 = 2.51; d_2 = 2.38$		−5.73 (−6.24)	−4.40 (−4.28)
1T_d-$ReSe_2$	$a_1 = 6.58; a_2 = 6.74$	$d_1 = 2.51; d_2 = 2.51$		−5.02 (−5.50)	−3.90 (−3.80)
TiS_3	$a_1 = 4.99; a_2 = 3.39$	$d_1 = 2.45; d_2 = d_3 = 2.49; d_4 = 2.65$		−4.37 (−4.33)	−4.05 (−3.29)
HfS_3	$a_1 = 5.09; a_2 = 3.58$	$d_1 = 2.55; d_2 = d_3 = 2.60; d_4 = 2.68$		−4.57 (−4.59)	−3.51 (−2.72)
$HfSe_3$	$a_1 = 5.40; a_2 = 3.71$	$d_1 = 2.69; d_2 = d_3 = 2.74; d_4 = 2.85$		−4.34 (−4.30)	−4.01 (−3.32)
ZrS_3	$a_1 = 5.14; a_2 = 3.62$	$d_1 = 2.60; d_2 = d_3 = 2.62; d_4 = 2.72$		−4.53 (−4.46)	−3.50 (−2.57)
$ZrSe_3$	$a_1 = 5.42; a_2 = 3.74$	$d_1 = 2.74; d_2 = d_3 = 2.76; d_4 = 2.88$		−4.24 (−4.21)	−3.96 (−3.26)

significantly as the VBM values increase and the band gap location of puckered phosphorene shifts to the Γ point. Finally, it should be noted that in addition to their monolayers, these group V materials can also form stable bilayer and layered 3D structures, where the puckered antimonene has a slightly distorted phase [57,58].

In Fig. 3(b) we present the complete band alignment properties of group V monolayers. In particular, puckered phosphorene and arsenene retain their Γ valley band edges even with increasing layer numbers. One can envision various type I or II Γ valley lateral heterostructures by controlling layer numbers. In addition, these group V puckered elements tend to have relatively low CBMs, ~ -4 eV, which allows them to form type I or II heterostructures with group IV and III-V compounds, which we discussed earlier—particularly those with a high VBM of ~ -4 eV.

C. Transition-metal dichalcogenides

So far we have discussed the monolayer structures of Group III, IV, and V elements and their compounds. Additionally,

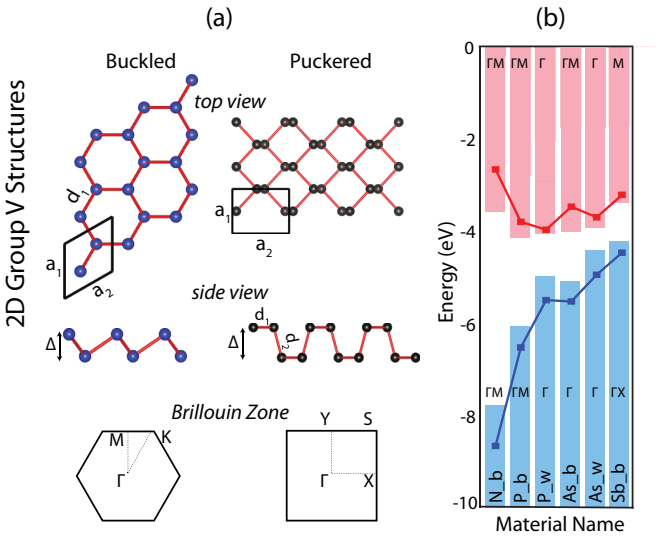

FIG. 3. (a) Stable crystalline structures (buckled and puckered) of group V elements and their corresponding hexagonal and rectangular BZ with high-symmetry points are shown. The relevant bond lengths and lattice parameters are indicated by a and d, respectively. (b) Same as Fig. 2(b), but for group V monolayers.

it is also possible to construct stable 2D materials using transition metals to form TMDs, which exhibit a versatile chemistry [13,14,64]. The general formula of a TMD is MX_2, in which M stands for a transition-metal atom and X is a chalcogen (S, Se, Te) [65]. Most common TMDs are either in 1T or 2H phases, where 1T and 2H refer to the structure of the lattices as exhibited in Fig. 4(a). In the 1T-MX_2 phase, the lattice is octahedral (Oh), while in the 2H-MX_2 phase it is trigonal prismatic (D3h). In addition, ReS_2 and $ReSe_2$ are observed with a distorted 1T crystal structure due to Peierls or Jahn-Teller distortions [66,67]. As shown

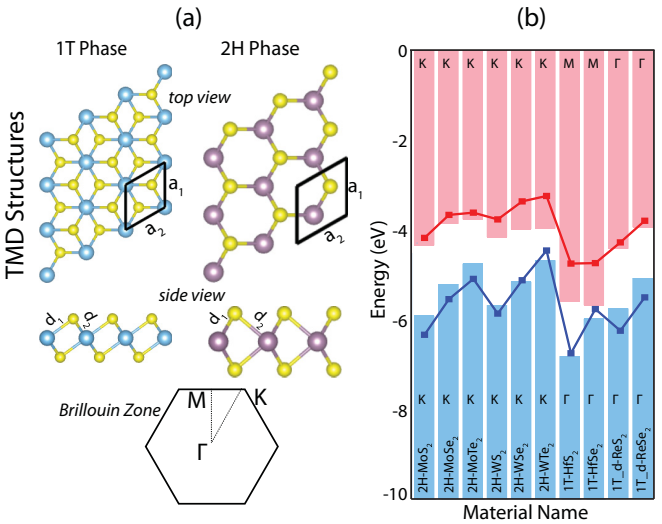

FIG. 4. (a) Stable crystalline structures (1T and 2H phases) of TMDs and their corresponding hexagonal BZ with high-symmetry points are shown. The relevant bond lengths and lattice parameters are indicated by a and d, respectively. Note that the structures of ReS_2 and $ReSe_2$ are in a distorted 1T phase. (b) Same as Fig. 2(b) but for TMDs.

in Fig. 4(b), monolayer MX_2 structures (M = Mo, W) are typically direct-band-gap semiconductors, whereas TiX_2 is metallic, hence not shown in this work. With the increase in the number of layers, the electronic structure of 2H-MX_2 changes from direct to indirect band gap and the band gap also decreases [68,69].

The relaxed geometries of TMDs show that as X goes from S to Te, the bond lengths and lattice constants increase slightly. Also, among these materials, MoX_2 and WX_2 have the closest lattice constants to each other, suggesting possible applications in various lateral heterostructures. In Fig. 4(b), we present the band alignment results of all of the stable MX_2 semiconductor phases. As a general trend, the VBM and CBM increase as X changes from S to Te, similar to the trend in the lattice constants. Also, it should be noted that among structures containing the same X atom, the CBM and VBM value of WX_2 is always the highest. This suggests the construction of type II heterostructures, for example by using WX_2 and MoX_2. As far as the **k**-space location of the band gaps is concerned, all of the M = Mo and M = W structures have direct band gaps at the K point. For the remaining materials, the VBM is always at the Γ point and CBM is at the M point if M = Hf, and at Γ for M = Re. It should be noted that for M = Re we have semiconductors with a direct band gap at the Γ point. These Re-based TMDs were also found to have a band gap that is relatively insensitive to the number of layers [66].

D. Transition-metal trichalcogenides

Another family of semiconducting monolayer materials is the transition-metal trichalcogenides (TMTs) which are layered structures with weak interlayer van der Waals

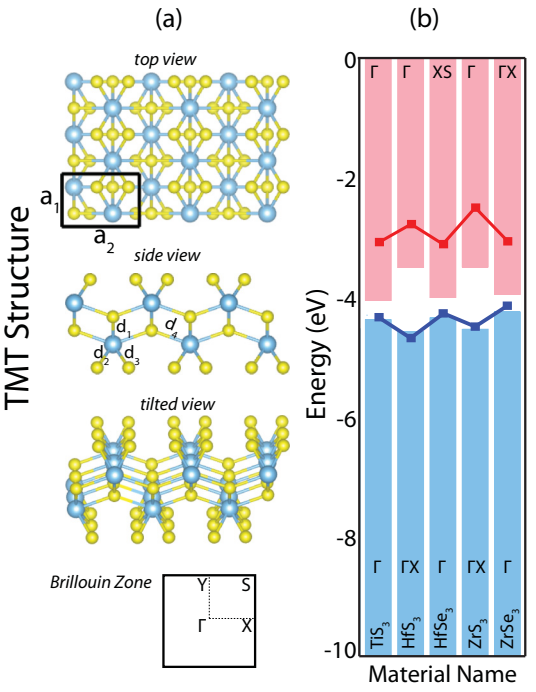

FIG. 5. (a) Stable crystalline structure of TMTs and its corresponding rectangular BZ with high-symmetry points are shown. The relevant bond lengths and lattice parameters are indicated by a and d, respectively. (b) Same as Fig. 2(b) but for TMTs.

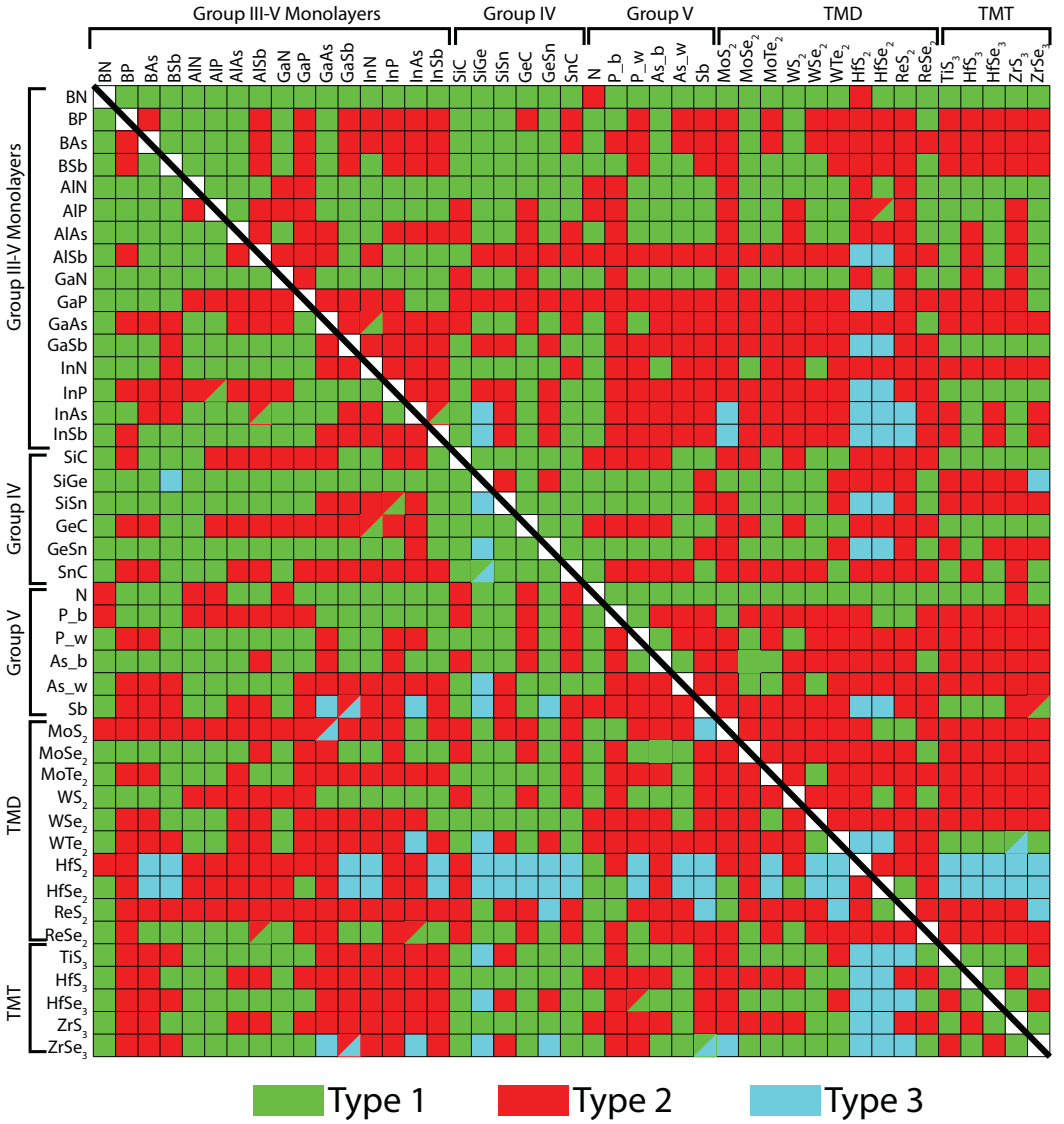

FIG. 6. Periodic table of heterostructures. Type I, II, and III heterostructures are represented by green, red, and blue boxes, respectively. The lower left and upper right of regions of the diagonal line present results calculated by PBE and HSE06, respectively. Two-colored boxes, which correspond to the same energy within the error range of our DFT study, indicate equal chances of two different types of heterostructures for the corresponding materials.

interactions. The general chemical formula for a TMT is MX_3, where M is the transition metal Ti, Zr, or Hf and X is a chalcogen, i.e., S, Se, or Te. They have monoclinic crystalline structures [70,71] with rectangular unit cells containing two metal and six chalcogen atoms, where each metal atom is connected to six chalcogen atoms as shown in Fig. 5(a). Previous experimental studies have reported the electronic properties of bulk TMTs [72–76].

In Fig. 5(b), we present the band alignment results for this family of monolayer semiconductors. Our calculations reveal that, among the semiconducting monolayers of TMTs, only TiS_3 is a direct band gap semiconductor where both the VBM and CBM are located at the Γ point. Using the PBE functional [42], TiS_3 has a fundamental gap of 0.32 eV and this increases to 1.04 eV when calculated by HSE06, which is comparable with the experimentally observed value of 1.10 eV [77–80]. Similarly, the band gaps of all TMTs studied here increase and get closer to their experimentally observed values when calculated with HSE06. They are all indirect gap semiconductors, having either the VBM or the CBM slightly offset from the Γ point. TMTs have a low CBM of about −4.5 eV, so they can be combined with high-VBM monolayers, such as HfS_2 and $HfSe_2$, to form type III heterostructures. It is also possible to construct type II heterostructures by combining appropriate TMTs with MoS_2 and ReS_2. Combining HfS_3 with $HfSe_2$ would make a type II heterostructure. Here we note that, for $HfSe_3$, the location of the CBM changes from XS to X when calculated by HSE06.

IV. PERIODIC TABLE OF HETEROSTRUCTURES

Having calculated the geometrical and electronic properties of all well-known two-dimensional semiconductors using a unified approach, we finally focus on establishing the complete

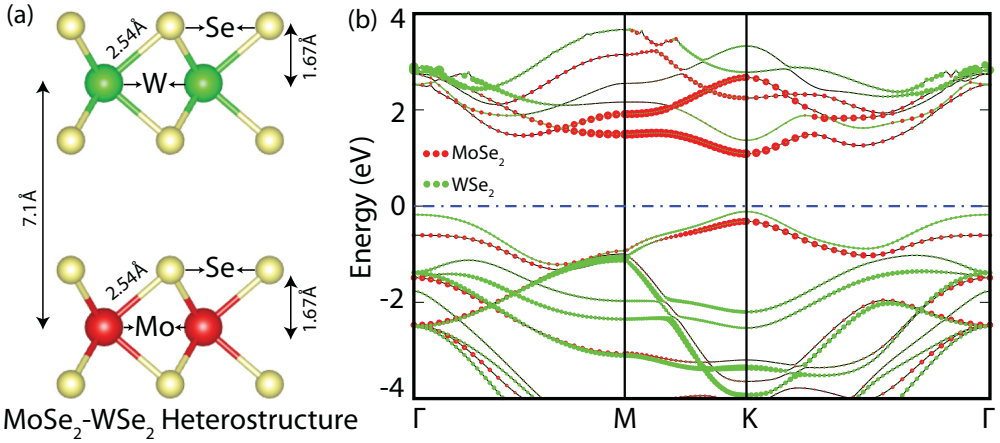

FIG. 7. (a) Geometrical parameters and (b) the electronic band structure of the $MoSe_2$-WSe_2 heterostructure. In the band structure, bands projected to $MoSe_2$ and WSe_2 layers are indicated with red (dark) and green (light) circles, respectively. The Fermi level is shown with blue dashed line.

set of heterostructure types that would form when any two of these materials are merged together, some of which were discussed above. For this, we use the criteria illustrated in Fig. 1. Namely, when material A and material B merge, the resulting heterostructure is type I if $VBM_A < VBM_B < CBM_B < CBM_A$, is type II if $VBM_A < VBM_B < CBM_A < CBM_B$, and type III if $VBM_A < CBM_A < VBM_B < CBM_B$. Using these criteria, we systematically present our results in the periodic table of heterostructures in Fig. 6, using both the PBE and HSE06 approaches. Accordingly, we mostly see type I heterostructures in group III-V and group IV compounds, where as type II heterostructures dominate as we move to group V, TMD, and TMT regions. Type III heterostructures can emerge in TMD and TMT regions of the periodic table. As evident from Figs. 2–5, the 2D materials family has CBM that mostly varies from −2 to −4 eV, and a VBM between −4 to −6 eV. Hence, the likelihood for the formation of type I and II naturally has higher occurrence, while type III tends to be rare. It should be noted that, for some rare cases the VBM of material A is equal to the CBM of material B (or vice versa) within the accuracy of our DFT results; which suggests that the type of the heterostructure can vary between two possibilities depending on other conditions. We also note that the presented results also depend on the type of density functional (i.e., PBE versus HSE06) used, as seen in Fig. 6.

The results presented here in the periodic table of heterostructures should provide a useful guidance for experimentalists in selecting suitable momentum-matched 2D materials for heterostructure design. As an example, we calculated the optimized stable geometry and the electronic band structure of the $MoSe_2$-WSe_2 heterostructure with AA stacking as shown Figs. 7(a) and 7(b). The bands projected to $MoSe_2$ and WSe_2 layers in the combined band diagram show that both $MoSe_2$ and WSe_2 layers preserve their isolated band structure characteristic. Both of them preserve the locations of their CBM and VBM at the K point, while their isolated band gaps increase from 1.34 eV to 1.39 eV for $MoSe_2$ and from 1.23 eV to 1.48 eV for WSe_2. This makes the overall system a type II heterostructure with a band gap of 1.21 at the K point, which is consistent with our prediction in Fig. 6. A similar comparison can easily be made for all of the 903 heterostructures presented in Fig. 6; however such a detailed comparison is computationally ambitious and beyond the scope of our current work. It should be noted that in the case of the $MoSe_2$-WSe_2 composite, the heterostructure has the same lattice constant as its constituents. However, this is may not be true in general for other heterostructures. In such lattice-mismatched cases, the constituent layers can have internal stress, in addition to other structural effects such as twist angle between the layers [81] which is more likely to modify their band structures slightly. These modifications must be taken into account while working with lattice-mismatched heterostructures.

V. CONCLUSION

In conclusion, we have presented a complete and comparative set of properties of well-known semiconductors including their structural and electronic properties. We identified possible types of heterostructures that can be realized using these materials. Using these unified results, we constructed a periodic table of heterostructures which provides a useful guidance for future experimental/theoretical studies. Additionally, the presented band alignment results and their band edges in momentum space using a consistent methodology provide a rich database for creating heterostructures with momentum space matching. In particular, we found that about half of the 2D semiconductors we surveyed have either (or both) the conduction and valence band edges at the zone center Γ; hence they can be excellent candidates in constructing momentum-matched heterostructures.

The electronic band diagrams of the materials studied in this paper are available as Supplemental Material [82].

ACKNOWLEDGMENTS

We acknowledge fruitful discussion with Dr. Mehmet Topsakal. J.G.A. and T.L. acknowledge partial support from NSF ECCS-1542202. S.J.K. was supported in part by the National Science Foundation (NSF) through the University of Minnesota MRSEC under Award No. DMR-1420013. The computational resources were provided by the Minnesota Supercomputing Institute (MSI).

[1] A. Geim and I. Grigorieva, Nature (London) **499**, 419 (2013).
[2] K. Novoselov and A. H. Castro Neto, Phys. Scr. **2012**, 014006 (2012).
[3] K. S. Novoselov, A. K. Geim, S. Morozov, D. Jiang, Y. Zhang, S. Dubonos, I. Grigorieva, and A. Firsov, Science **306**, 666 (2004).
[4] A. K. Geim and K. S. Novoselov, Nat. Mater. **6**, 183 (2007).
[5] D. Pacile, J. Meyer, C. O. Girit, and A. Zettl, Appl. Phys. Lett. **92**, 133107 (2008).
[6] C. R. Dean, A. F. Young, I. Meric, C. Lee, L. Wang, S. Sorgenfrei, K. Watanabe, T. Taniguchi, P. Kim, K. Shepard *et al.*, Nat. Nanotechnol. **5**, 722 (2010).
[7] S. Cahangirov, M. Topsakal, E. Aktürk, H. Şahin, and S. Ciraci, Phys. Rev. Lett. **102**, 236804 (2009).
[8] P. Vogt, P. De Padova, C. Quaresima, J. Avila, E. Frantzeskakis, M. C. Asensio, A. Resta, B. Ealet, and G. Le Lay, Phys. Rev. Lett. **108**, 155501 (2012).
[9] V. O. Özçelik, E. Durgun, and S. Ciraci, J. Phys. Chem. Lett. **5**, 2694 (2014).
[10] J. W. Suk, R. D. Piner, J. An, and R. S. Ruoff, ACS Nano **4**, 6557 (2010).
[11] V. O. Özçelik, S. Cahangirov, and S. Ciraci, Phys. Rev. Lett. **112**, 246803 (2014).
[12] B. Yang, S. Shaikhutdinov, and H.-J. Freund, Surf. Sci. **632**, 9 (2015).
[13] P. Joensen, R. Frindt, and S. R. Morrison, Mater. Res. Bull. **21**, 457 (1986).
[14] C. Ataca and S. Ciraci, J. Phys. Chem. C **115**, 13303 (2011).
[15] B. Radisavljevic, A. Radenovic, J. Brivio, V. Giacometti, and A. Kis, Nat. Nanotechnol. **6**, 147 (2011).
[16] S. Tongay, J. Zhou, C. Ataca, K. Lo, T. S. Matthews, J. Li, J. C. Grossman, and J. Wu, Nano Lett. **12**, 5576 (2012).
[17] S. Nakamura, M. Senoh, N. Iwasa, and S.-i. Nagahama, Jpn. J. Appl. Phys. **34**, L797 (1995).
[18] Y. Arakawa and A. Yariv, IEEE J. Quantum Electron. **22**, 1887 (1986).
[19] P. S. Zory, *Quantum Well Lasers* (Academic Press, 1993).
[20] J. D. Werking, C. R. Bolognesi, L.-D. Chang, C. Nguyen, E. L. Hu, and H. Kroemer, IEEE Electron Device Lett. **13**, 164 (1992).
[21] A. Levi and T. Chiu, Appl. Phys. Lett. **51**, 984 (1987).
[22] F. Capasso, S. Sen, A. C. Gossard, A. L. Hutchinson, and J. H. English, IEEE Electron Device Lett. **7**, 573 (1986).
[23] S. O. Koswatta, S. J. Koester, and W. Haensch, IEEE Trans. Electron Devices **57**, 3222 (2010).
[24] J. Meyer, C. Hoffman, F. Bartoli, and L. Ram-Mohan, Appl. Phys. Lett. **67**, 757 (1995).
[25] Y. Zhang, W. Ma, Y. Cao, J. Huang, Y. Wei, K. Cui, and J. Shao, IEEE J. Quantum Electron. **47**, 1475 (2011).
[26] J. Faist, F. Capasso, D. L. Sivco, C. Sirtori, A. L. Hutchinson, and A. Y. Cho, Science **264**, 553 (1994).
[27] C.-H. Lee, G.-H. Lee, A. M. Van Der Zande, W. Chen, Y. Li, M. Han, X. Cui, G. Arefe, C. Nuckolls, T. F. Heinz *et al.*, Nat. Nanotechnol. **9**, 676 (2014).
[28] L. Britnell, R. Ribeiro, A. Eckmann, R. Jalil, B. Belle, A. Mishchenko, Y.-J. Kim, R. Gorbachev, T. Georgiou, S. Morozov *et al.*, Science **340**, 1311 (2013).
[29] W. Zhang, C.-P. Chuu, J.-K. Huang, C.-H. Chen, M.-L. Tsai, Y.-H. Chang, C.-T. Liang, Y.-Z. Chen, Y.-L. Chueh, J.-H. He *et al.*, Sci. Rep. **4**, 3826 (2014).
[30] F. Withers, O. Del Pozo-Zamudio, A. Mishchenko, A. Rooney, A. Gholinia, K. Watanabe, T. Taniguchi, S. Haigh, A. Geim, A. Tartakovskii *et al.*, Nat. Mater. **14**, 301 (2015).
[31] P. Rivera, J. R. Schaibley, A. M. Jones, J. S. Ross, S. Wu, G. Aivazian, P. Klement, K. Seyler, G. Clark, N. J. Ghimire *et al.*, Nat. Commun. **6**, 6242 (2015).
[32] E. Calman, C. Dorow, M. Fogler, L. Butov, S. Hu, A. Mishchenko, and A. Geim, Appl. Phys. Lett. **108**, 101901 (2016).
[33] D. Ruzmetov, K. Zhang, G. Stan, B. Kalanyan, G. R. Bhimanapati, S. M. Eichfeld, R. A. Burke, P. B. Shah, T. P. O'Regan, F. J. Crowne *et al.*, ACS Nano **10**, 3580 (2016).
[34] J. Yuan, S. Najmaei, Z. Zhang, J. Zhang, S. Lei, P. M. Ajayan, B. I. Yakobson, and J. Lou, ACS Nano **9**, 555 (2015).
[35] Y. Gong, J. Lin, X. Wang, G. Shi, S. Lei, Z. Lin, X. Zou, G. Ye, R. Vajtai, B. I. Yakobson *et al.*, Nat. Mater. **13**, 1135 (2014).
[36] V. O. Özçelik, E. Durgun, and S. Ciraci, J. Phys. Chem. C **119**, 13248 (2015).
[37] K. Kim, S. Larentis, B. Fallahazad, K. Lee, J. Xue, D. C. Dillen, C. M. Corbet, and E. Tutuc, ACS Nano **9**, 4527 (2015).
[38] J. Kang, S. Tongay, J. Zhou, J. Li, and J. Wu, Appl. Phys. Lett. **102**, 012111 (2013).
[39] C. Gong, H. Zhang, W. Wang, L. Colombo, R. M. Wallace, and K. Cho, Appl. Phys. Lett. **103**, 053513 (2013).
[40] S. Grimme, J. Comput. Chem. **27**, 1787 (2006).
[41] P. E. Blöchl, Phys. Rev. B **50**, 17953 (1994).
[42] J. P. Perdew, K. Burke, and M. Ernzerhof, Phys. Rev. Lett. **77**, 3865 (1996).
[43] G. Kresse and J. Furthmüller, Phys. Rev. B **54**, 11169 (1996).
[44] J. Paier, M. Marsman, K. Hummer, G. Kresse, I. C. Gerber, and J. G. Ángyán, J. Chem. Phys. **124**, 154709 (2006).
[45] K. Novoselov, D. Jiang, F. Schedin, T. Booth, V. Khotkevich, S. Morozov, and A. Geim, Proc. Natl. Acad. Sci. USA **102**, 10451 (2005).
[46] K. V. Emtsev, A. Bostwick, K. Horn, J. Jobst, G. L. Kellogg, L. Ley, J. L. McChesney, T. Ohta, S. A. Reshanov, J. Röhrl *et al.*, Nat. Mater. **8**, 203 (2009).
[47] V. O. Özçelik and S. Ciraci, J. Phys. Chem. C **117**, 15327 (2013).
[48] D. Kecik, C. Bacaksiz, R. T. Senger, and E. Durgun, Phys. Rev. B **92**, 165408 (2015).
[49] V. O. Özçelik and S. Ciraci, Phys. Rev. B **91**, 195445 (2015).
[50] A. Onen, D. Kecik, E. Durgun, and S. Ciraci, Phys. Rev. B **93**, 085431 (2016).
[51] H. Şahin, S. Cahangirov, M. Topsakal, E. Bekaroglu, E. Akturk, R. T. Senger, and S. Ciraci, Phys. Rev. B **80**, 155453 (2009).
[52] L. Li, Y. Yu, G. J. Ye, Q. Ge, X. Ou, H. Wu, D. Feng, X. H. Chen, and Y. Zhang, Nat. Nanotechnol. **9**, 372 (2014).
[53] H. Liu, A. T. Neal, Z. Zhu, Z. Luo, X. Xu, D. Tománek, and P. D. Ye, ACS Nano **8**, 4033 (2014).
[54] Z. Zhu and D. Tománek, Phys. Rev. Lett. **112**, 176802 (2014).
[55] T. Low, A. S. Rodin, A. Carvalho, Y. Jiang, H. Wang, F. Xia, and A. H. Castro Neto, Phys. Rev. B **90**, 075434 (2014).
[56] A. Rodin, A. Carvalho, and A. H. Castro Neto, Phys. Rev. Lett. **112**, 176801 (2014).
[57] V. O. Özçelik, O. Ü. Aktürk, E. Durgun, and S. Ciraci, Phys. Rev. B **92**, 125420 (2015).
[58] O. Ü. Aktürk, V. O. Özçelik, and S. Ciraci, Phys. Rev. B **91**, 235446 (2015).

[59] S. Zhang, Z. Yan, Y. Li, Z. Chen, and H. Zeng, Angew. Chem., Int. Ed. **54**, 3112 (2015).
[60] C. Kamal and M. Ezawa, Phys. Rev. B **91**, 085423 (2015).
[61] R. R. Q. Freitas, R. Rivelino, F. de Brito Mota, C. M. C. de Castilho, A. Kakanakova-Georgieva, and G. K. Gueorguiev, J. Phys. Chem. C **119**, 23599 (2015).
[62] L. Kou, C. Chen, and S. C. Smith, J. Phys. Chem. Lett. **6**, 2794 (2015).
[63] R. J. Wu, M. Topsakal, T. Low, M. C. Robbins, N. Haratipour, J. S. Jeong, R. M. Wentzcovitch, S. J. Koester, and K. A. Mkhoyan, J. Vac. Sci. Technol. A **33**, 060604 (2015).
[64] J. N. Coleman, M. Lotya, A. O'Neill, S. D. Bergin, P. J. King, U. Khan, K. Young, A. Gaucher, S. De, R. J. Smith *et al.*, Science **331**, 568 (2011).
[65] M. Chhowalla, H. S. Shin, G. Eda, L.-J. Li, K. P. Loh, and H. Zhang, Nat. Chem. **5**, 263 (2013).
[66] S. Tongay, H. Sahin, C. Ko, A. Luce, W. Fan, K. Liu, J. Zhou, Y.-S. Huang, C.-H. Ho, J. Yan *et al.*, Nat. Commun. **5**, 3252 (2014).
[67] D. Wolverson, S. Crampin, A. S. Kazemi, A. Ilie, and S. J. Bending, ACS Nano **8**, 11154 (2014).
[68] W. S. Yun, S. W. Han, S. C. Hong, I. G. Kim, and J. Lee, Phys. Rev. B **85**, 033305 (2012).
[69] Q. H. Wang, K. Kalantar-Zadeh, A. Kis, J. N. Coleman, and M. S. Strano, Nat. Nanotechnol. **7**, 699 (2012).
[70] S. Furuseth, L. Brattas, and A. Kjekshus, Acta Chem. Scand. **29**, 623 (1975).
[71] L. Brattas and A. Kjekshus, Acta Chem. Scand. **26**, 3441 (1972).
[72] E. Finkman and B. Fisher, Solid State Commun. **50**, 25 (1984).
[73] S. Kikkawa, M. Koizumi, S. Yamanaka, Y. Onuki, and S. Tanuma, Phys. Status Solidi A **61**, K55 (1980).
[74] I. Gorlova, V. Y. Pokrovskii, S. Zybtsev, A. Titov, and V. Timofeev, J. Exp. Theor. Phys. **111**, 298 (2010).
[75] S. Srivastava and B. Avasthi, J. Mater. Sci. **27**, 3693 (1992).
[76] F. Levy and H. Berger, J. Cryst. Growth **61**, 61 (1983).
[77] I. Ferrer, J. Ares, J. Clamagirand, M. Barawi, and C. Sánchez, Thin Solid Films **535**, 398 (2013).
[78] I. Ferrer, M. Maciá, V. Carcelén, J. Ares, and C. Sánchez, Energy Procedia **22**, 48 (2012).
[79] J. O. Island, M. Barawi, R. Biele, A. Almazán, J. M. Clamagirand, J. R. Ares, C. Sánchez, H. S. van der Zant, J. V. Álvarez, R. D'Agosta *et al.*, Adv. Mater. **27**, 2595 (2015).
[80] J. O. Island, R. Biele, M. Barawi, J. M. Clamagirand, J. R. Ares, C. Sanchez, H. S. van der Zant, I. J. Ferrer, R. D'Agosta, and A. Castellanos-Gomez, Sci. Rep. **6**, 22214 (2016).
[81] A. M. van der Zande, J. Kunstmann, A. Chernikov, D. A. Chenet, Y. You, X. Zhang, P. Y. Huang, T. C. Berkelbach, L. Wang, F. Zhang *et al.*, Nano Lett. **14**, 3869 (2014).
[82] See Supplemental Material at http://link.aps.org/supplemental/10.1103/PhysRevB.94.035125 for the electronic band diagrams of the 2D materials discussed in this paper.